



An Aligned Orbit for the Young Planet V1298 Tau b

Marshall C. Johnson^{1,2}, Trevor J. David^{3,4}, Erik A. Petigura⁵, Howard T. Isaacson⁶, Judah Van Zandt⁵, Ilya Ilyin⁷, Klaus Strassmeier⁷, Matthias Mallonn⁷, George Zhou⁸, Andrew W. Mann⁹, John H. Livingston¹⁰, Rodrigo Luger³, Fei Dai¹¹, Lauren M. Weiss¹², Teo Močnik¹³, Steven Giacalone⁶, Michelle L. Hill¹⁴, Malena Rice¹⁵, Sarah Blunt¹⁶, Ryan Rubenzahl¹⁶, Paul A. Dalba^{14,17,19}, Gilbert A. Esquerdo¹⁸, Perry Berlind¹⁸, Michael L. Calkins¹⁸, and Daniel Foreman-Mackey³

¹ Las Cumbres Observatory, 6740 Cortona Drive, Suite 102, Goleta, CA 93117, USA; johnson.7240@osu.edu

² Department of Astronomy, The Ohio State University, 4055 McPherson Laboratory, 140 West 18th Avenue, Columbus, OH 43210 USA

³ Center for Computational Astrophysics, Flatiron Institute, 162 5th Avenue New York, NY 10010, USA

⁴ Department of Astrophysics, American Museum of Natural History, 200 Central Park West, New York, NY 10024, USA

⁵ Department of Physics and Astronomy, University of California, Los Angeles, 430 Portola Plaza, Box 951547, Los Angeles, CA 90095, USA

⁶ Department of Astronomy, University of California, Berkeley, 501 Campbell Hall #3411, Berkeley, CA 94720, USA

⁷ Leibniz-Institut für Astrophysik Potsdam (AIP), An der Sternwarte 16, D-14482 Potsdam, Germany

⁸ Centre for Astrophysics, University of Southern Queensland, USQ Toowoomba, West Street, QLD 4350, Australia

⁹ Department of Physics and Astronomy, University of North Carolina at Chapel Hill, 120 E. Cameron Avenue, Phillips Hall CB3255, Chapel Hill, NC 27599, USA

¹⁰ Department of Astronomy, University of Tokyo, 7-3-1 Hongo, Bunkyo-ku, Tokyo 113-0033, Japan

¹¹ Division of Geological and Planetary Sciences, California Institute of Technology, 1200 E California Boulevard, Pasadena, CA, 91125, USA

¹² Department of Physics, University of Notre Dame, 225 Nieuwland Science Hall, Notre Dame, IN 46556, USA

¹³ Gemini Observatory/NSF's NOIRLab, 670 N. A'ohoku Place, Hilo, HI 96720, USA

¹⁴ Department of Earth and Planetary Sciences, University of California Riverside, 900 University Avenue, Riverside, CA 92521, USA

¹⁵ Department of Astronomy, Yale University, New Haven, CT 06511, USA

¹⁶ Astronomy Department, California Institute of Technology, 1200 East California Boulevard, Pasadena CA 91125, USA

¹⁷ Department of Astronomy and Astrophysics, University of California, Santa Cruz, CA 95064, USA

¹⁸ Center for Astrophysics | Harvard & Smithsonian, 60 Garden Street, Cambridge, MA 02138, USA

Received 2021 October 7; revised 2022 March 10; accepted 2022 March 16; published 2022 May 4

Abstract

The alignment of planetary orbits with respect to the stellar rotation preserves information on their dynamical histories. Measuring this angle for young planets helps illuminate the mechanisms that create misaligned orbits for older planets, as different processes could operate over timescales ranging from a few megayears to a gigayear. We present spectroscopic transit observations of the young exoplanet V1298 Tau b; we update the age of V1298 Tau to be 28 ± 4 Myr based on Gaia EDR3 measurements. We observed a partial transit with Keck/HIRES and LBT/PEPSI, and detected the radial velocity anomaly due to the Rossiter–McLaughlin effect. V1298 Tau b has a prograde, well-aligned orbit, with $\lambda = 4^{+7}_{-10}$ deg. By combining the spectroscopically measured $v \sin i_*$ and the photometrically measured rotation period of the host star we also find that the orbit is aligned in 3D, $\psi = 8^{+4}_{-7}$ deg. Finally, we combine our obliquity constraints with a previous measurement for the interior planet V1298 Tau c to constrain the mutual inclination between the two planets to be $i_{\text{mut}} = 0^\circ \pm 19^\circ$. This measurements adds to the growing number of well-aligned planets at young ages, hinting that misalignments may be generated over timescales of longer than tens of megayears. The number of measurements, however, is still small, and this population may not be representative of the older planets that have been observed to date. We also present the derivation of the relationship between i_{mut} , λ , and i for the two planets.

Unified Astronomy Thesaurus concepts: Exoplanets (498); Exoplanet dynamics (490); High resolution spectroscopy (2096); Starspots (1572); Pre-main sequence (1289)

Supporting material: machine-readable table

1. Introduction

Planets are formed in circumstellar disks, which themselves form as a result of angular momentum conservation during the collapse of protostellar cores. The angular momentum vectors of stars and protoplanetary disks should therefore be aligned at the start of the planet formation process. Even the modest tilt of six degrees between the Sun’s spin axis and the mean angular momentum plane of the solar system is seen as a curiosity

demanding a physical explanation (Kuiper 1951). Proposed mechanisms capable of producing this tilt include asymmetric infall or torques from mass concentrations in the collapsing core (Tremaine 1991), encounters with other stars in the birth cluster (Heller 1993), the presence of an undiscovered planet in the solar system (Bailey et al. 2016; Gomes et al. 2017), and a misalignment between the solar spin and mean solar wind axes (Spalding 2019).

In contrast with the mildly misaligned solar system, exoplanets are routinely found on well-aligned, grossly misaligned, polar, and even retrograde orbits (Dawson & Johnson 2018). How and when stellar spin–orbit misalignments arise are open questions. Some spin–orbit misalignments may be primordial, the result of, for example, torquing of the protoplanetary disk by a distant companion, nearby star, or

¹⁹ NSF Astronomy and Astrophysics Postdoctoral Fellow.

Original content from this work may be used under the terms of the Creative Commons Attribution 4.0 licence. Any further distribution of this work must maintain attribution to the author(s) and the title of the work, journal citation and DOI.

other gas aggregation in the birth cluster (Heller 1993; Thies et al. 2011; Batygin et al. 2011, 2020; Batygin 2012; Spalding & Batygin 2014). Early-stage misalignments may also arise from asymmetric, variable, and turbulent accretion (Tremaine 1991; Bate et al. 2010; Fielding et al. 2015), magnetic star–disk interactions (Lai et al. 2011; Foucart & Lai 2011; Batygin & Adams 2013; Lai 2014; Spalding & Batygin 2014, 2015), or planet–disk interactions (Millholland & Batygin 2019; Su & Lai 2020). Still other misalignments may emerge long after the planet has formed, as a result of dynamical interactions with other planets or a companion star (Fabrycky & Tremaine 2007; Wu et al. 2007; Naoz et al. 2011; Storch et al. 2014).

By measuring exoplanet obliquities for systems of varying ages it may be possible to determine when spin–orbit misalignments typically arise, which in turn can help to determine the dominant mechanism(s) producing misalignments. If misalignments are predominantly generated by disk tilting, then misaligned orbits should be seen for planets of all ages. If, on the other hand, misalignments are typically generated by slower mechanisms like secular chaos or the Kozai–Lidov mechanism, then misaligned orbits should begin to appear at ages of order hundreds of megayears. Planet–planet scattering should operate on intermediate timescales of tens of megayears. Obliquity measurements for young exoplanets are particularly intriguing as those systems should more closely reflect the initial conditions of a given planetary system. In particular, some planets which start off misaligned may become realigned over time due to tidal interactions with the host star (Albrecht et al. 2012).

Here we report on the obliquity of V1298 Tau b (aka EPIC 210818897b or K2-309 b), a moderately irradiated (24 day period), Jupiter-sized exoplanet transiting a young solar analog with an age of 20–30 Myr (David et al. 2019a). The planet is one of at least four transiting planets in the system (David et al. 2019b), and Suárez Mascareño et al. (2021) recently measured a mass of $0.64 M_J$ for this planet. Given the presence of multiple transiting planets, a low mutual inclination between the planets is implied, but there is no requirement that the stellar spin axis be aligned with the orbital angular momentum vectors of the planets.

Our analysis is based on contemporaneous high-resolution time-series spectroscopy acquired with the Keck/HIRES, LBT/PEPSI, and FLWO/TRES spectrographs (defined in Sections 2.1.2 and 2.1.3), covering a single transit event. We also include transit photometry from the K2 mission and Spitzer Space Telescope to accurately constrain the planet’s ephemeris and other transit parameters. We use both the Rossiter–McLaughlin (RM) and Doppler Tomography techniques to attempt to infer the obliquity of V1298 Tau b.

The remainder of the paper is organized as follows. In Section 2 we describe our spectroscopic observations and auxiliary time-series photometry. We describe our analysis methods in Section 3 and discuss our findings in the context of other exoplanet studies in Section 4. Finally, we present our conclusions in Section 5.

2. Observations

2.1. Spectroscopic Observations

Below we describe the spectroscopic observations which form the basis of our analysis. The radial velocities derived from these observations are listed in Table 1.

Table 1
Radial Velocities of V1298 Tau

Date (BJD)	RV (m s ⁻¹)	Error (m s ⁻¹)	Instrument
2458780.853237	182.2	6.2	HIRES
2458780.858724	176.9	6.1	HIRES
2458780.864210	160.9	6.2	HIRES
2458780.869662	179.4	6.0	HIRES
2458780.881040	163.0	5.9	HIRES

Note. Table 1 is published in its entirety in the machine-readable format. A portion is shown here for guidance regarding its form and content.

(This table is available in its entirety in machine-readable form.)

2.1.1. Keck/HIRES

We observed a partial transit of V1298 Tau b on 2019 October 24 UT with the 10 m Keck I telescope on Maunakea, Hawaii, USA, and the HIRES spectrograph (Vogt et al. 1994). HIRES is a cross-dispersed échelle spectrograph. We used the C2 decker, with a slit of 0''.861 width and 14''.0 height, yielding a resolving power of $R \sim 60,000$ and the ability to subtract background light including scattered moonlight and night sky emission lines. The spectra span from 3646 to 7984 Å, although the velocities are derived from the 5000–6000 Å region.

Our observations began 5.7 hr before transit and continued through the first 75% of the transit, terminating at twilight. These were interrupted only by obtaining a template spectrum of V1298 Tau during the pre-transit phase (which is included in our Doppler tomographic time series but not our radial velocity (RV) time series), and a brief interruption during transit while the target passed through the zenith and the telescope tracking could not keep up. During this time we obtained 54 spectra, two of which were template spectra without the I₂ cell in the light path, and the remaining 52 of which used the I₂ cell. RVs were derived from the HIRES spectra using the California Planet Survey pipeline described in Howard et al. (2010). We included an additional eight HIRES RVs acquired within 20 days of the transit night in order to train a Gaussian process, as described in Section 3.3. These RVs were acquired as part of an ongoing program and derived in an identical fashion to those acquired during the transit night.

2.1.2. LBT/PEPSI

We observed the same transit with the Potsdam Echelle Polarimetric and Spectroscopic Instrument (PEPSI; Strassmeier et al. 2015) at the 2×8.4 m Large Binocular Telescope (LBT) on Mount Graham, Arizona, USA. We used PEPSI’s $R = 120,000$ mode and cross-dispersers III and V (covering 4800–5441 Å and 6278–7419 Å). We acquired 24 spectra (with exposures of 900 s). We began observing 4.4 hr before ingress, but were only able to observe the first 25% of the transit before morning twilight due to LBT’s more easterly location with respect to Keck.

The data reduction was performed with the Spectroscopic Data Systems pipeline, adapted to the PEPSI data calibration flow and image-specific content. It was based upon the pipeline described in Ilyin (2000) and a recent description is given in Strassmeier et al. (2018).

The specific steps of image processing included bias subtraction and variance estimation of the source images, super-master flat-field correction for the CCD spatial noise, échelle order definition from the tracing flats, scattered light subtraction, and a wavelength solution for the ThAr images. The pipeline then performed optimal extraction of image slicers and cosmic ray spikes elimination of the target image, wavelength calibration, and merging slices in each order, and normalization to the master flat-field spectrum to remove CCD fringes and blaze function. Finally, it performed a global 2D fit to the continuum of the normalized image, and rectification of all spectral orders in the image to a 1D spectrum for a given cross-disperser.

The spectra from two sides of the telescope were averaged with weights into one spectrum and corrected for the barycentric velocity of the solar system. The wavelength scale was preserved for each pixel as given by the wavelength solution without rebinning. The wavelength solution used about 3000 ThAr lines and had the error of the fit at the image center of 4 m s^{-1} .

The time-series spectra were cross-correlated in the blue and red arms separately with respect to the first three averaged spectra which were used as the reference spectrum. A pre-selected spectral region in the red with low telluric contamination was used for cross-correlation. It used a weighted linear regression fit of the reference spectrum to the observed one for every RV offset of the re-sampled reference spectrum. The accuracy of the offset was defined by the curvature of the cross-correlation peak and χ^2_ν of the regression fit.

2.1.3. FLWO 1.5 m/TRES

We obtained 21 epochs of observations of V1298 Tau using the Tillinghast Reflector Echelle Spectrograph (TRES; Fűrész 2008) on the 1.5 m telescope at the Fred Lawrence Whipple Observatory (FLWO), Arizona, USA. Nine epochs were obtained over the two weeks prior to the transit event on 24 October 2019 UT, and 12 were obtained on the night of the transit. TRES is a fiber-fed echelle with a spectral resolving power of $R \approx 44,000$ over the wavelength range 3850–9100 Å. Each epoch consists of three consecutive exposures that are median combined to reduce the impact of cosmic rays, and are bracketed by a set of ThAr hollow cathode lamp exposures that provide the wavelength solution to the spectrum. The spectra are calibrated and extracted as per Buchhave et al. (2012). To measure the RVs, we derived line profiles from each spectrum via a least-squares deconvolution analysis (Donati et al. 1997), and fit the broadening profiles with a joint kernel describing the effects of the Doppler shift, rotational, macroturbulent, and instrumental broadening. The derived velocities are presented in Table 1 and Figure 1.

2.2. Photometric Observations

In addition to our spectroscopic observations, we used two photometric data sets in our fits in order to accurately derive the planetary ephemeris. We describe these data below.

2.2.1. K2

The Kepler space telescope observed V1298 Tau between 2015 Feb 7 and 2015 Apr 23 UT during Campaign 4 of its extended K2 mission (Howell et al. 2014). We used K2 photometry in conjunction with our RVs to determine accurate

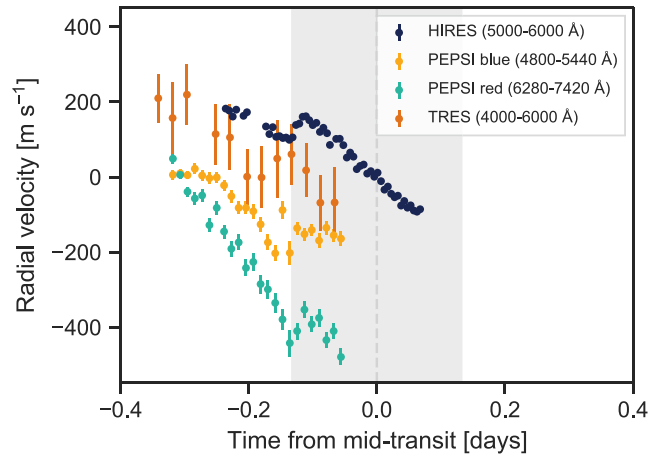


Figure 1. Comparison of time-series radial velocities (RVs) acquired by different spectrographs on the night of the transit of V1298 Tau b. Offsets and trends of varying slopes between instruments are apparent. The gray shaded band indicates the predicted transit window. The chromaticity of the RV trend is apparent from the PEPSI data. We note that wavelength ranges indicated are the approximate regions from which RV information is extracted, and not necessarily the complete wavelength ranges of the spectra.

and robust uncertainties on the sky-projected obliquity and related transit parameters. We used the flattened light curve from David et al. (2019b), which in turn used the EVEREST 2.0 pipeline (Luger et al. 2016, 2018) to optimize the photometric aperture and correct the light curve for instrumental systematics using pixel-level decorrelation.

2.2.2. Spitzer

A partial transit of V1298 Tau b was observed in the IRAC2 ($4.5 \mu\text{m}$) channel on the Spitzer Space Telescope on 2019 June 1 UT (J. H. Livingston et al., in preparation). We direct the reader to that paper for details on the Spitzer data processing procedures. In this work we are only concerned with accurately measuring the planet’s ephemeris and other transit parameters, and we use the corrected light curve presented by those authors.

From the David et al. (2019b) ephemeris, based only on K2 data from 2015, the predicted times (in BJD) of ingress, mid-transit, and egress on the night of our observations were ≈ 2458780.82665 , 2458780.96040 , and 2458781.09415 , respectively. Including the Spitzer data instead constrained these times to be 2458780.95530 , 2458781.08905 , and 2458781.22280 (again in BJD). Therefore, including the Spitzer constraints shifts the transit three hours later on our night of observations.

3. Analysis

3.1. Reassessment of V1298 Tau’s Age

With the recent arrival of Gaia Data Early Data Release 3 (EDR3; Gaia Collaboration et al. 2016, 2021), it should be possible to derive a more precise age measurement than was possible in David et al. (2019a). To this end, we used the Group 29 membership list from Luhman (2018) with updated photometry and parallaxes from Gaia EDR3. We removed stars with $\text{RUWE} > 1.2$, as these are more likely to be binaries (Ziegler et al. 2020). We compared the resulting color-magnitude diagram (CMD) to predictions from the PARSECv1.2S models (Bressan et al. 2012) assuming solar abundance. To account for both binaries and non-member interlopers, we perform the comparison using a mixture model

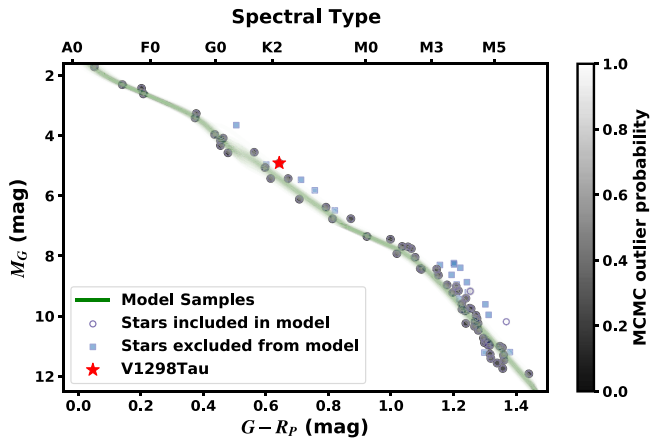


Figure 2. Example comparison of likely members of Group 29 to a model isochrone from PARSEC. Each point is a star from Luhman (2018), shaded by their probability of being part of the outlier distribution (the second model in the mixture). Squares are targets that were excluded from the fit due to a high RUWE, although including them made no difference (they were captured as outliers in the mixture). The green lines are 100 random model samples from the Markov chain Monte Carlo posteriors. V 1298 Tau is denoted as a red star. Approximate spectral types are listed on the top axis.

following Hogg et al. (2010) and described in more detail in A. W. Mann et al. (2022, in preparation). To briefly summarize, we compared photometry for candidate members to a two-component model; the first component was a single-star single-aged population drawn from the isochrone (for a given $E(B - V)$ and age), and the second component an outlier population described by an offset from the first component (Y_B) and a variance around that offset (V_B). There were two additional free parameters, one to capture underestimated uncertainties, differential reddening, and small age spreads (f), and one for the amplitude of the second population (P_B) such that a pure single-star, single-age population should have $P_B = 0$. All parameters evolved under uniform priors. We performed the comparison in an Markov chain Monte Carlo (MCMC) framework using emcee with 50 walkers and 100,000 steps following a burn-in of 10,000 steps.

We show the resulting fit in Figure 2 (see also Figure 9 for a corner plot), which yielded an age of 30 ± 3 Myr. This uncertainty does not fully account for systematic errors in the models or uncertainties arising from the sample selection. The latter may be especially important, as V 1298 Tau is not on the membership list from Luhman (2018) and the greater Taurus–Auriga association is likely a mix of many populations (Krolikowski et al. 2021). To test for model errors, we repeated the process using models from the Dartmouth Stellar Evolution Program (Dotter et al. 2008) with magnetic enhancement (Feiden & Chaboyer 2012). To test for problems with the sample selection, we repeated the comparison with each model grid using a sample of stars with tangential velocities within 2 km s^{-1} and locations within 25 pc of V 1298 Tau selected using the FriendFinder²⁰ algorithm (Tofflemire et al. 2021). FriendFinder stars were closer (kinematically and spatially) to V 1298 Tau, and hence more likely to be from the same initial cloud, but this selection also contained some non-member interlopers (evident from a low CMD position). Fortunately, our mixture model simply models these stars as outliers and they have a small or negligible impact on the final age.

²⁰ <https://github.com/adamkraus/Comove>

Table 2
Results of Line Profile Fit

Parameter	Value
Measured Parameters	
$v \sin i_*$ (km s^{-1})	$24.87^{+0.19}_{-0.21}$
v_{int} (km s^{-1})	$6.20^{+0.16}_{-0.17}$
q_1	$0.351^{+0.104}_{-0.099}$
q_2	$0.166^{+0.079}_{-0.067}$
Derived Parameters	
g_1	$0.193^{+0.071}_{-0.074}$
g_2	$0.4^{+0.12}_{-0.13}$

Note. Parameters derived from the fit to the line profile of V1298 Tau. v_{int} is the intrinsic width of a Gaussian line of each stellar surface element. q are the triangularly sampled limb-darkening parameters per Kipping (2013), while g are the corresponding quadratic limb-darkening parameters.

For all four fits, the estimated age was between 25 and 32 Myr. Based on this, we adopt a conservative age of 28 ± 4 Myr, consistent with earlier 20–30 Myr assessments (Luhman 2018; David et al. 2019b). Notably, V 1298 Tau sits above the CMD in all fits, although it is consistent with the scatter seen around the model sequence for other members.

3.2. Stellar Rotational Velocity

Obtaining an accurate measurement of the spin–orbit misalignment from the RM effect depends critically upon having an accurate measurement of the projected stellar rotational velocity $v \sin i_*$. V1298 Tau is sufficiently rapidly rotating that we can spectroscopically resolve the rotationally broadened line profile and directly measure $v \sin i_*$.

We use the higher-resolution PEPSI data for this purpose. We extracted the average line profile from the PEPSI spectra as described in Section 3.4. We fit these data using the misttborn package²¹ (e.g., Johnson et al. 2017; Dholakia et al. 2019). We produced a model rotationally broadened line profile as described in Johnson et al. (2014); briefly, we assume that the line profile from each stellar surface element is a Gaussian appropriately Doppler shifted according to the RV of the surface element assuming solid body rotation. We assume a quadratic limb-darkening law, and use the triangular sampling method of Kipping (2013). We then numerically integrate over a Cartesian grid on the surface of the star. misttborn uses the affine-invariant MCMC package emcee (Foreman-Mackey et al. 2013) to produce posterior distributions for the parameters.

We present the results from this fit in Table 2. Our value of $v \sin i_* = 24.87^{+0.19}_{-0.21} \text{ km s}^{-1}$ is consistent with but more precise than previous measurements (David et al. 2019a). We adopt this value for the remainder of the analyses in this paper.

3.3. RVRM Analysis

We show our radial velocities on the night of the transit in Figure 1. It is apparent from this figure that we detect the transit with both HIRES and PEPSI, and that the orbit is prograde; there is a sharp positive deviation in the RVs from both instruments during ingress. However, there is also a large out-of-transit slope in the RVs, which varies from instrument to

²¹ <https://github.com/captain-exoplanet/misttborn>

instrument and, indeed, even between the RVs derived from the red and blue arms of PEPSI. We ascribe this RV trend to starspots rotating across the face of V1298 Tau. Starspots are chromatic, and will therefore have different influences on RVs measured at different wavelengths.

We jointly modeled the RVs and time-series photometry using the `starry` 1.1.2 (Luger et al. 2019) and `exoplanet` 0.5.1 (Foreman-Mackey et al. 2019, 2021) packages. Stellar surface brightness and velocity field variations are modeled as an expansion of spherical harmonics in `starry`. These variations, and their derivatives, are computed analytically so `starry` models can be easily incorporated in gradient-based optimization and inference procedures such as Hamiltonian Monte Carlo (HMC), No U-Turns Sampling (NUTS), and variational inference. Detailed descriptions of the application of `starry` to RM measurements are provided in Bedell et al. (2019) and Montet et al. (2020).

The inferred sky-projected obliquity is sensitive to the underlying RV trend. This is particularly true for the data set in consideration as the RVs only cover a partial transit (complete transits are rarely observable from a single site due to the long orbital period and transit duration). In an idealized, perfectly quiet star the RV trend arises from the reflex motion of the star due to all orbiting companions. In the present case, V1298 Tau has prominent starspots which induce apparent RV variations that are more than an order of magnitude larger ($\sim 200 \text{ m s}^{-1}$ in semi-amplitude) than the expected Doppler semi-amplitudes of any of the known planets in the system. Consequently, in the modeling that follows we neglect reflex motions due to the planets.

In order to investigate the sensitivity of the inferred obliquity on the assumed RV trend we explored a number of different approaches to modeling the underlying RV variations: (1) a linear trend, (2) a quadratic trend, and (3) a quasiperiodic Gaussian process (GP). For the GP kernel we selected the quasiperiodic rotation term kernel implemented in `exoplanet`, a combination of two stochastically driven simple harmonic oscillators which has been shown to successfully reproduce stellar variability (Angus et al. 2018). Further details about this kernel and its associated hyperparameters are presented in David et al. (2019b). We note that in the GP modeling of the RVs, we chose not to use the PEPSI red data as they showed a much steeper out-of-transit slope than the PEPSI blue, HIRES, and TRES data and thus were not well described by our model, which adopts a single GP amplitude across all instruments.

For the linear and quadratic trend models we jointly fit only the Keck/HIRES RVs (as these are the most precise and present the clearest detection of the RM anomaly) along with the flattened K2 and Spitzer light curves. For the GP, we included RVs acquired within 20 days of the RM observations in order to train the GP. We included constant offsets and jitter parameters for each individual instrument in the RV data set as well as for the K2 and Spitzer time series. Since starspot crossings affect the transit depths of the K2 light curve, we allowed the jitter parameter for that data set to scale linearly with the transit depth in order to account for the excess noise in transit. In all models we assumed a linear ephemeris (i.e., we did not include transit timing variations) across the RV, Spitzer, and K2 data sets; we were able to obtain a good fit to all five individual transit events using this assumption. We also assumed a single R_p/R_* value for all data sets. K2 and the

RV spectrographs use broadband optical passbands, and the Spitzer transit depth has been found to be consistent with the K2 transit depth at the 1σ level (J. H. Livingston et al., in preparation). We also neglect eccentricity in the orbit of planet b as transit modeling and orbit-crossing constraints suggest it is small, < 0.3 (David et al. 2019b).

The rotation period of V1298 Tau was precisely measured from the K2 light curve via GP regression ($P_{\text{rot}} = 2.87 \pm 0.02 \text{ d}$; David et al. 2019b). We incorporate this information into our model by placing a Gaussian prior on the inferred equatorial rotation period, where that quantity is derived as $P_{\text{rot,eq}} = 2\pi R_*/v_{\text{eq}}$, and R_* is a directly sampled parameter. The equatorial velocity, v_{eq} is derived from $v \sin i_*$ (a free parameter) and $\sin i_*$ (derived from $\cos i_*$, which is sampled from a uniform distribution between 0 and 1) using $v_{\text{eq}} = v \sin i_*/\sin i_*$.

We note that a limitation of this model is that it does not explicitly account for surface differential rotation, as we do not know what latitude(s) gave rise to the K2 brightness modulations. Differential rotation may be as high as $\sim 0.4 \text{ rad d}^{-1}$ for young stars (e.g., Marsden et al. 2006, 2011). For reference, differential rotation of 0.2 rad d^{-1} in V1298 Tau would result in a pole-to-equator difference of 0.2–0.3 days in the rotation period, an order of magnitude larger than the uncertainty reported from the GP regression. To account for the uncertainty introduced by differential rotation, for each model we tested two different P_{rot} priors in the HMC sampling: Gaussian priors centered on the photometrically determined rotation period with widths of 0.2 days and 0.02 days (the concentrated prior).

Notably, the constraints on the rotation period, $v \sin i_*$, and R_* allow the stellar inclination to be inferred which, combined with the planet's orbital inclination and sky-projected obliquity, allows for derivation of the spin-orbit angle (see Equation (9) of Fabrycky & Winn 2009).

To infer robust uncertainties on the parameters in our models we used the NUTS sampler as implemented in PyMC3 3.11.4 (Salvatier et al. 2016). After finding the maximum a posteriori model we initiated the sampler using 5000 tuning steps, a target acceptance fraction of 95%, and two chains each with 2500 draws from the posterior. Convergence was assessed using the Gelman–Rubin statistic (Gelman & Rubin 1992).

For a selection of models we show the mean model predictions and uncertainty bands in Figures 3 and 4. We summarize the inferred obliquities from these fits in Table 3 and Figure 5. Detailed MCMC summary statistics for the preferred model (the quasiperiodic GP with a tight P_{rot} prior, using only the HIRES data) are presented in Table 5, and we show the posterior distributions in Figure 10. The priors used in the RVRM analysis are summarized in Table 4. The data and code needed to reproduce our RVRM analysis are publicly available through GitHub.²² The contents of this GitHub repository as well as the MCMC posteriors have been deposited to Zenodo: doi:10.5281/zenodo.6394450.

The adopted trend model does have a significant effect upon the derived obliquity, as shown in Figure 5. Although the orbit is clearly prograde, the choice of trend model impacts the inferred value of the sky-projected spin-orbit misalignment λ at the $\sim 10^\circ$ – 20° level, and some of the distributions have tails to values of $|\lambda|$ as high as $\sim 60^\circ$.

²² <https://github.com/trevordavid/obliquity>

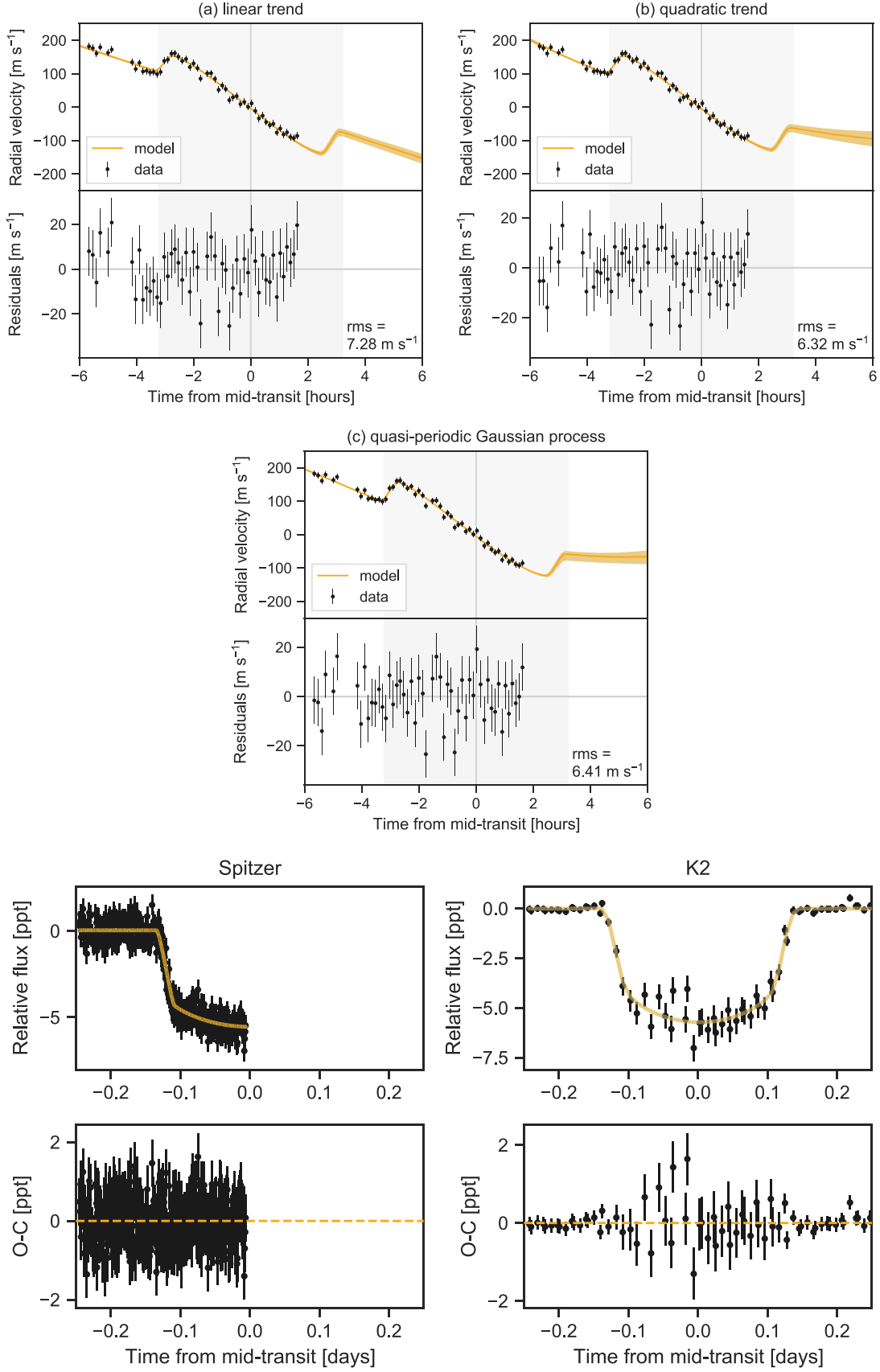


Figure 3. Top: median model predictions and the 68% percentile error bands for the (a) linear, (b) quadratic, and (c) quasiperiodic Gaussian process (GP) RV trend models. The data shown are from Keck/HIRES. The mean model residuals are plotted in the bottom panels. Bottom: best-fit models for the Spitzer (left) and *K2* (right) photometry. The data and models are shown in the top panels, and the residuals in the bottom panels. The large scatter in transit in the *K2* data is likely due to starspot crossings.

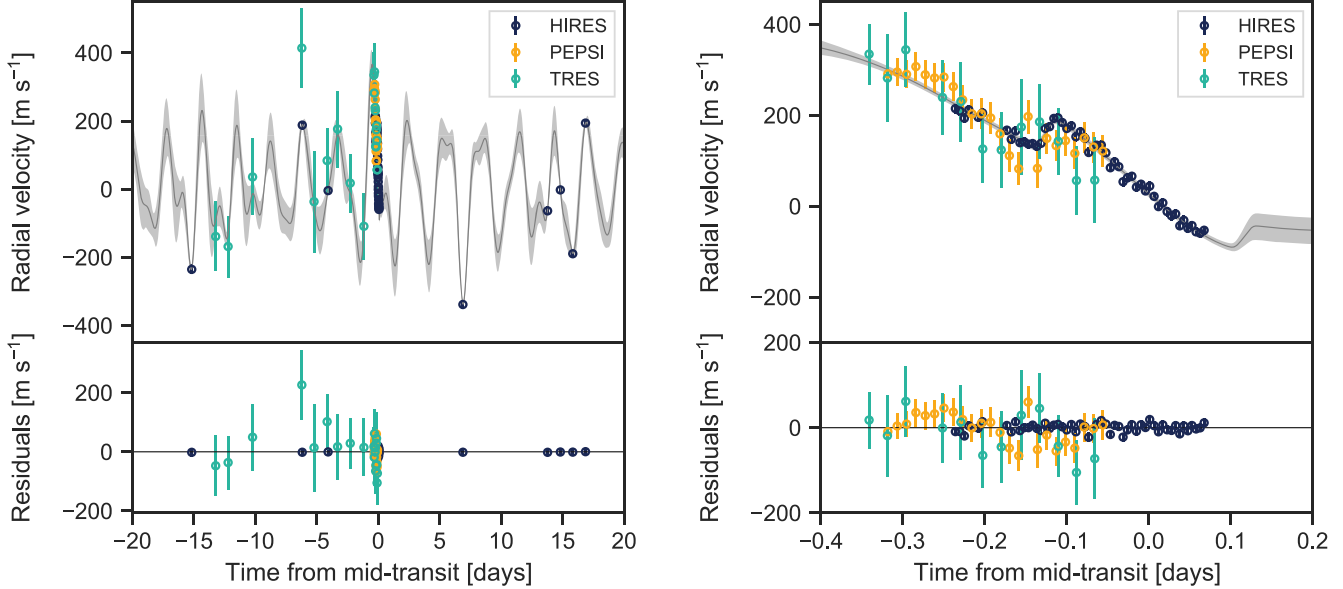


Figure 4. Mean model prediction and the 68% percentile error band (gray) for the quasiperiodic GP + RM fit to the combined HIRES, PEPSI blue, and TRES data sets with a tight P_{rot} prior. The data have been mean-subtracted and the mean model residuals are plotted in the lower panels. At left is the RV time series centered around the the Rossiter–McLaughlin (RM) observation night and at right is a zoom-in of the RM sequence.

Table 3
Inferred Obliquities from the RVRM Analyses

Model	Instruments	λ (deg)	ψ (deg)
Linear trend	HIRES	-22^{+9}_{-8}	23^{+10}_{-10}
Linear trend, tight P_{rot} prior	HIRES	-10^{+4}_{-6}	12^{+5}_{-5}
Quadratic trend	HIRES	-9^{+8}_{-7}	14^{+6}_{-9}
Quadratic trend, tight P_{rot} prior	HIRES	-1^{+5}_{-6}	6^{+3}_{-4}
Quasiperiodic GP	HIRES	-2^{+11}_{-16}	15^{+12}_{-12}
Quasiperiodic GP, tight P_{rot} prior	HIRES	4^{+7}_{-10}	8^{+4}_{-7}
Quasiperiodic GP	HIRES,	8^{+20}_{-23}	16^{+10}_{-14}
	PEPSI, TRES		
Quasiperiodic GP, tight P_{rot} prior	HIRES, PEPSI, TRES	10^{+12}_{-16}	12^{+8}_{-12}

Note. Values quoted are the medians and 68% highest density intervals from the posteriors. Adopted values in bold.

We ultimately adopt the GP models as our preferred solution; this model most carefully accounts for the RV trend, accounting for all of the information that we have on the stellar RV variability over timescales of hours to weeks. Additionally, we adopt the tight P_{rot} prior as this best encompasses prior knowledge of the system, but note that using the looser prior instead does not qualitatively change the results. Although the residuals for the transit RVs in this model are slightly larger than for the quadratic model, the difference is small (9 cm s^{-1}).

3.4. Doppler Tomographic Analysis

V1298 Tau is sufficiently rapidly rotating ($v \sin i_* \sim 24 \text{ km s}^{-1}$) that we can spectroscopically resolve the rotationally broadened line profile. The RVRM effect arises from the perturbation to the line profile due to the missing light from the planetary transit; the centroid shift due to this perturbation results in the RV anomaly during transit that we detected in Section 3.3. Due to V1298 Tau’s rapid rotation, we can hope to

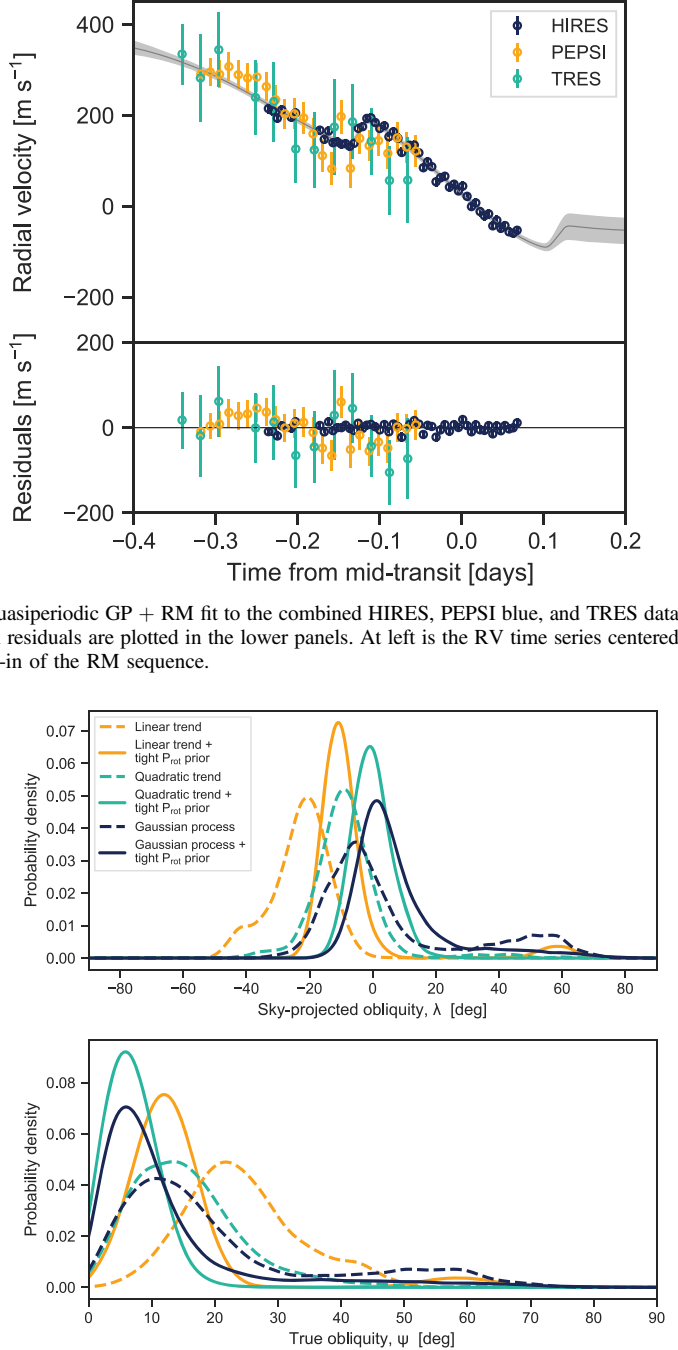


Figure 5. Comparison of posterior densities in sky-projected obliquity (top) and obliquity (bottom) for several of the RVRM models described in Section 3.3. Posteriors shown are from fits to the HIRES data and have been smoothed using Gaussian kernel density estimation for clarity.

directly measure this line profile perturbation in the time-series line profiles. This method is typically known as Doppler tomography (e.g., Albrecht et al. 2007; Collier Cameron et al. 2010; Johnson et al. 2014). Compared to the RM technique where we model the shifts in the line centroids, in Doppler tomography we instead directly model the line shape.

Our methodology for extracting the average line profiles from the time-series spectra was largely the same as that used in Johnson et al. (2014, 2015, 2017, 2018). In short, we used the least-squares deconvolution method (Donati et al. 1997), fitting a model produced by convolving a line profile with a

picket fence of δ functions at the wavelengths of the spectral lines to the data. We first fit for the depths of the individual spectral lines, and then for the line profile itself. We perform these fits to the data on an order-by-order basis; the final extracted line profile from a spectrum is the weighted average of these order-by-order line profiles, weighted based on the signal-to-noise and total equivalent width of lines in each order.

We used the full available bandwidth of PEPSI (4800–5441 Å and 6278–7419 Å) to extract the line profiles. For the HIRES data we extracted line profiles only from the blue and red chip data (covering 3646–4790 Å and 6549–7984 Å, respectively); the green chip data are heavily impacted by iodine absorption lines and therefore not usable for the Doppler tomographic analysis. Additionally, in order to increase the signal-to-noise, we binned together sets of three consecutive HIRES spectra before extracting the line profiles. We also do not consider the TRES spectra in this analysis because they are too low signal-to-noise.

We show our time-series line profile residuals in Figure 6. The line profile residuals are dominated by two streaks corresponding to two spot complexes moving across the stellar surface during the observations. These are most obvious in the PEPSI data, but are also present in the HIRES data. These corroborate the spotted nature of the star as being the source of the trend seen in the RV data. The track of the planet is not obvious by eye.

Our efforts to model out the line profiles in the combined data set and detect the planetary transit in the Doppler tomographic data have not yet borne fruit. We defer a full quantitative analysis of these data to a future publication.

We can, however, analyze the spot complexes themselves. We have two clearly detected spot complexes. The distributions of spots on a stellar surface can inform knowledge of the magnetic geometry. The spot longitude ϕ can easily be measured from the line profiles as

$$\sin \phi = \frac{v}{v \sin i_*} \quad (1)$$

where $\phi = 0$ is defined to be the sub-observer longitude.

We measure the spot longitudes from each of the pre-transit PEPSI spectra by fitting a Gaussian profile to the spots in the time-series line profile residuals. We fit the residuals from each spectrum separately, and take the mean and standard deviation of the spectrum where both spots were fit successfully as the measurement. We thus estimate a longitudinal separation between the two spots of $\Delta\phi = 42^\circ \pm 4^\circ$. There is no apparent trend in $\Delta\phi$ over the course of the observations, which could be caused by differential rotation. The motion of the spots is consistent with the photometric P_{rot} determined by David et al. (2019b). The time coverage of the observations is also too short to perform a full inversion to determine the overall surface spot distribution and determine the latitudes of the spots.

On the Sun, sunspots are often separated by 180° of longitude (Berdugina & Usoskin 2003). Although it is certainly possible that the 45° separation between the two spot complexes we see on V1298 Tau could be a coincidence, it could also hint at a non-solar-like dynamo. More observations of V1298 Tau would be required to test this hypothesis, to determine whether a 45° separation is typical. We note, however, that Feinstein et al. (2021) did not see any large spot complexes in their data, obtained a few months after our observations.

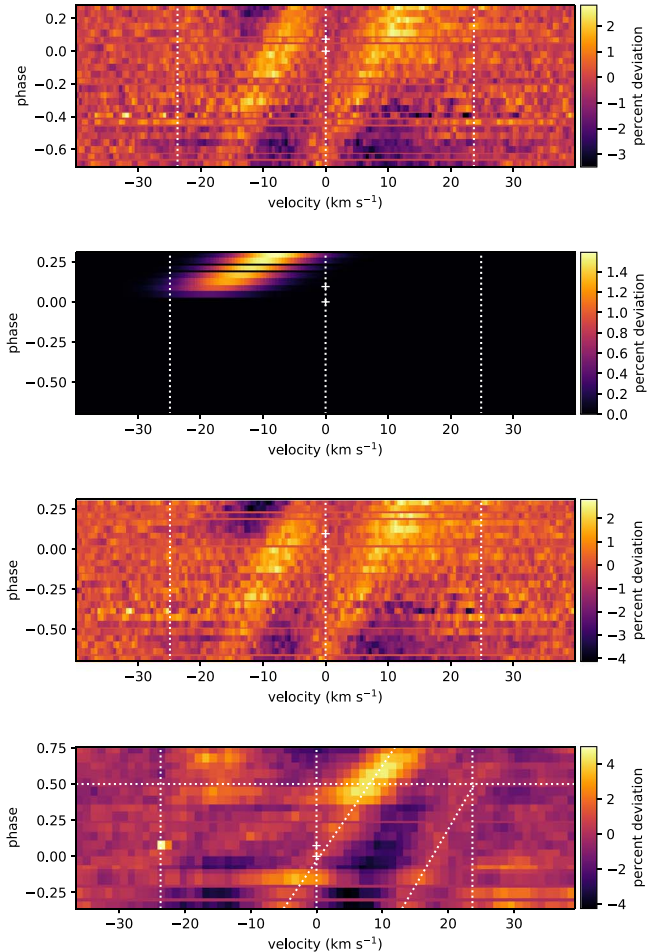


Figure 6. Doppler tomographic data from PEPSI (top three panels) and HIRES (bottom). All plots show the time-series line profile residuals, i.e., each horizontal line shows the deviation of the line profile from the average line profile at that time. Time increases from bottom to top; units are such that ingress = 0 and egress = 1. The vertical dotted lines show $v = 0, \pm v \sin i_*$, the horizontal dotted line the time of mid-transit, and the two small plus signs first and second contact. In the HIRES plot we also show two slanted dotted lines to guide the eye along the spot signatures, which are less obvious than in the PEPSI data.

In principle we could also measure the physical size of the spot complexes from the velocity space extension of the line profile perturbations. Even with the $R = 120,000$ PEPSI data, however, the spot signatures are of similar size to the instrumental broadening profile and so we consider them to be unresolved. Nonetheless, the instrumental resolution of 2.5 km s^{-1} corresponds to a best latitude resolution of $\sim 6^\circ$, which allows us to estimate an upper limit on the spot complex size of $< 0.15 R_\odot$.

4. Discussion

V1298 Tau b joins a growing number of planets in young stellar associations with measured spin-orbit angles, including DS Tuc Ab (Zhou et al. 2020; Montet et al. 2020; Benatti et al. 2021), AU Mic b (Hirano et al. 2020; Martioli et al. 2020; Palle et al. 2020; Addison et al. 2021b), HD 63433 b (Mann et al. 2020) and c (Dai et al. 2020), HIP 67522 b (Heitzmann et al. 2021), and V1298 Tau b's sister planet V1298 Tau c (Feinstein et al. 2021). Spin-orbit angles have also been determined for

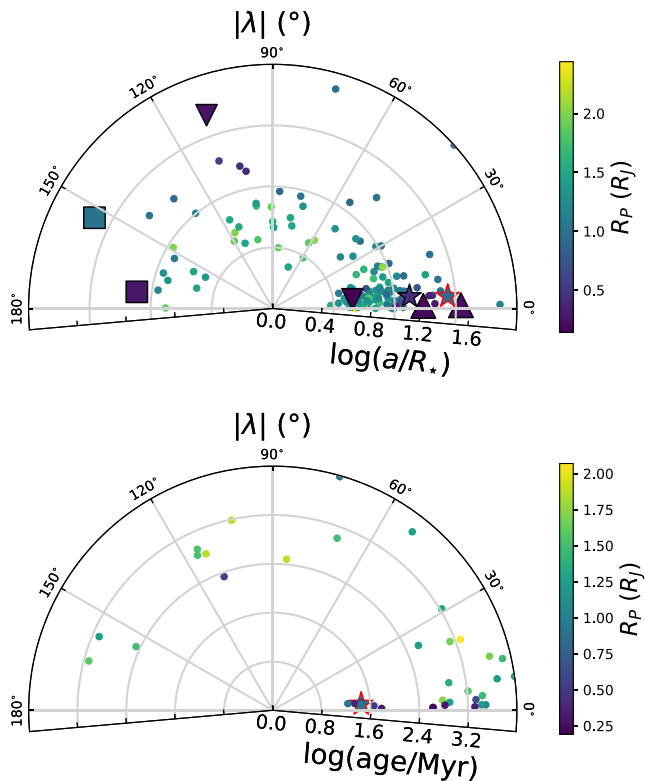


Figure 7. Measurement of the sky-projected spin–orbit misalignment of V1298 Tau b in context with measurements from the literature. Top: all published spin–orbit misalignments, shown as a function of the scaled semimajor axis a/R_* . The color scale shows the planetary radius. We highlight V1298 Tau b as the red-bordered star, and also show as larger symbols the four systems with published spin–orbit misalignment measurements for more than one planet: V1298 Tau (stars), HD 63433 (upward triangles), K2-290 (squares), and HD 3167 (downward triangles). Note that K2-290 is consistent with coplanarity, as the uncertainty on the measurement of λ for the inner planet is large (Hjorth et al. 2021), while HD 3167 is highly non-coplanar (Bourrier et al. 2021). Bottom: spin–orbit misalignments as a function of age; young planets are toward the center, older planets toward the edge. As has been noted by other recent works (e.g., Heitzmann et al. 2021), all of the young planets (<100 Myr age) with published measurements are aligned. However, the number of such planets is small. Again, V1298 Tau b is highlighted.

several planets transiting young field stars, including Kepler-63 b (Sanchis-Ojeda et al. 2013), TOI-942 b (Wirth et al. 2021), KELT-9 b (Gaudi et al. 2017; Ahlers et al. 2020), KELT-20 b (Lund et al. 2017), and TOI-1431 b/MASCARA-5 b (Addison et al. 2021a). The aforementioned planets in young associations, TOI-942 b, and KELT-20 b, have all been found to have aligned orbits, while Kepler-63 b, KELT-9 b, and TOI-1431 b/MASCARA-5 b are on polar orbits. We show this population in Figure 7. Thus, it appears that at least some spin–orbit misalignments can arise in the first few hundred megayears. Furthermore, the recent discovery of two planets on retrograde orbits around a field star is challenging to explain with post-formation evolution (Hjorth et al. 2021).

V1298 Tau b, with an orbital period of 24 days, is also among the longest-period planets for which the spin–orbit angle has been measured, as can be seen in the top panel of Figure 7.

The low obliquity of V1298 Tau b suggests that the various theoretical mechanisms proposed to produce primordial spin–orbit misalignments were not important enough to produce a gross misalignment in the system. Notably, there is no known stellar companion to the V1298 Tau system (David et al. 2019a).

We cannot rule out mild misalignments like that of the solar system. Of course, it is still possible that those same mechanisms may be important for some fraction of planetary systems.

There are now six planets in five systems with ages between 15 and 60 Myr with spin–orbit angle measurements, all of which are aligned. Although these are still small-number statistics, and a quantitative assessment will have to wait for the accumulation of more measurements, it appears that the majority of young systems are well aligned. If this trend is borne out by observations of more young planets, it could suggest that misaligned orbits are typically generated by dynamical mechanisms with longer timescales like secular chaos or the Kozai–Lidov effect.

It is unclear, however, how the young planet population relates to the older planets that account for most of the spin–orbit misalignment measurements to date. Most of the young planets do not have measured masses, and only HIP 67522 b and V1298 Tau b are near Jupiter-radius; meanwhile, two of the five young systems have multiple transiting planets. Furthermore, V1298 Tau hosts two planets with masses close to that of Jupiter with periods of 40 days or less (Suárez Mascareño et al. 2021), again setting it apart for the bulk of the spin–orbit misalignment sample. Only the HIP 67522 b system could resemble the hot Jupiters that make up most of the field-age sample. Conversely, only a few older small and multi-planet systems have spin–orbit measurements. The multi-planet systems are generally well-aligned, with a few exceptions (Huber et al. 2013; Dalal et al. 2019; Hjorth et al. 2021), while lonely hot Neptunes may be more commonly misaligned (Winn et al. 2010; Bourrier et al. 2018; Rubenzahl et al. 2021). The aligned young planets may simply belong to a population that is typically aligned at all ages. More spin–orbit measurements for both young planets and older small planets, as well as mass measurements for the young planets, are needed to draw firm conclusions.

4.1. Mutual Inclination and System Architecture

The recent measurement of the spin–orbit angle for V1298 Tau c by Feinstein et al. (2021) presents an opportunity to constrain the mutual inclination of the two planets. They found that planet c is consistent with an aligned orbit, with $\lambda_c = 5^\circ \pm 15^\circ$. We show a schematic of the transit geometry of the system in Figure 8.

The mutual inclination between two planets with known values of i and λ can be expressed as

$$\cos i_{\text{mut}} = \sin i_1 \sin i_2 \cos(\lambda_1 - \lambda_2) + \cos i_1 \cos i_2 \quad (2)$$

where i_{mut} is the mutual inclination between the two planets. We present the derivation of Equation (2) in Appendix A.

We find a mutual inclination between V1298 Tau b and c of $i_{\text{mut}} = 0^\circ \pm 19^\circ$. Although this is not particularly constraining, it confirms that these two planets are consistent with a coplanar configuration. This is expected given the presence of four transiting planets in this system (David et al. 2019b).

Future observations of both planets, as well as the other planets orbiting V1298 Tau, to more precisely measure the spin–orbit misalignment could enable meaningful constraints on the mutual inclinations and overall architecture of this system.

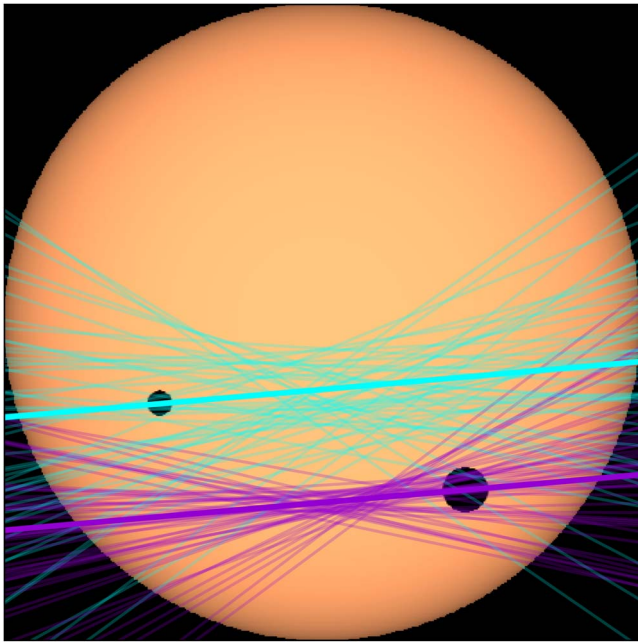


Figure 8. Schematic of the transit geometry of V1298 Tau b (large disk, purple) and c (small disk, cyan). The thick lines show the best-fit transit chords for each planet from this work and Feinstein et al. (2021), respectively, while the thin lines show 50 random draws from the posterior distributions; note that we only consider uncertainties in λ and b , which are the parameters that directly govern the path of the planet across the stellar disk.

5. Conclusions

We summarize our key findings below.

1. The RM effect is clearly detected during a partial transit of V1298 Tau b, indicating a prograde orbit and a likely low orbital obliquity for the planet. V1298 Tau b is one of the youngest and coolest exoplanets for which the orbital obliquity has been constrained.
2. From modeling of the partial RM curve we find the inferred sky-projected obliquity of V1298 Tau, with respect to the orbit of planet b, is sensitive to the underlying RV trend. A range of obliquities are compatible with the data but, for most assumed models of the RV trend, sampling from the posterior distributions indicates that the highest posterior density is at low or moderate obliquities ($|\lambda| \lesssim 20^\circ$) and the data are compatible with an obliquity of zero. For our most realistic model of the stellar RV trend we find a sky-projected obliquity of $\lambda = 4^{+7}_{-10}$ deg and an obliquity of $\psi = 8^{+4}_{-7}$ deg.
3. Combining our obliquity constraints with those of the interior planet V1298 Tau c published in Feinstein et al. (2021) we constrained the mutual inclination of the two planets to be $i_{\text{mut}} = 0^\circ \pm 19^\circ$. The available data are thus consistent with a coplanar configuration and a low stellar obliquity, as expected from formation within a circumstellar disk.
4. Using newly available data from Gaia DR3, we revise the age of V1298 Tau to 28 ± 4 Myr.
5. At the epoch of our spectroscopic observations, we find the existence of two spot complexes on V1298 Tau separated by $\Delta\phi = 42^\circ \pm 4^\circ$ of longitude.

6. From our joint fits of the RVs and photometry we derive a new, more precise transit ephemeris for V1298 Tau b:

$$T_{\text{mid}} = 2458781.0835 \pm 0.0013$$

$$P = 24.141341 \pm 0.000023 \text{ days.}$$

7. RVs derived from the PEPSI spectrograph clearly demonstrate the chromaticity of the underlying RV trend, which we attribute to rotation of the inhomogeneous stellar surface. We find RV slopes of $\sim 45 \text{ m s}^{-1} \text{ hr}^{-1}$ in the blue arm (4800–5441 Å) and $\sim 95 \text{ m s}^{-1} \text{ hr}^{-1}$ in the red arm (6278–7419 Å). It is notable that a steeper trend is observed at redder optical wavelengths, counter to expectations from how stellar activity scales with wavelength (e.g., Tran et al. 2021). One possible explanation is that the PEPSI red radial velocities are derived from a larger set of spectral lines that are particularly prominent in starspots, thereby biasing the radial velocities more strongly in the red compared to the blue data.
8. We demonstrate that an intra-night RV precision of $6\text{--}7 \text{ m s}^{-1}$ is achievable on V1298 Tau, a highly active pre-main-sequence star, using Keck/HIRES with the iodine cell and the California Planet Search RV pipeline.

The same time-series spectra through the course of a transit used for spin-orbit misalignment measurements are also often usable for transmission spectroscopy to investigate the planetary atmosphere and exosphere. We analyze the time-variable H α line profile of V1298 Tau in our data in a companion paper (T. J. David et al. in preparation).

Thanks to Adina Feinstein, Ben Montet, and Elisabeth Newton for useful discussions. We thank the other observers who contributed some of our observations or helped with the planning of the observations: David Latham, Samuel Quinn, and Andrew Howard. Thanks to Josh Walawender for supporting our Keck observations.

This work was supported by a NASA Keck PI Data Award through JPL RSA 1634873. P.D. is supported by a National Science Foundation (NSF) Astronomy and Astrophysics Postdoctoral Fellowship under award AST-1903811.

Some of the data presented herein were obtained at the W. M. Keck Observatory, which is operated as a scientific partnership among the California Institute of Technology, the University of California and the National Aeronautics and Space Administration. The Observatory was made possible by the generous financial support of the W. M. Keck Foundation. This research has made use of the Keck Observatory Archive (KOAs), which is operated by the W. M. Keck Observatory and the NASA Exoplanet Science Institute (NExScI), under contract with the National Aeronautics and Space Administration. The LBT is an international collaboration among institutions in the United States, Italy and Germany. The LBT Corporation partners are: The Ohio State University; LBT Beteiligungsgesellschaft, Germany, representing the Max Planck Society, the Astrophysical Institute Potsdam, and Heidelberg University; The University of Arizona on behalf of the Arizona university system; Istituto Nazionale di Astrofisica, Italy; The Research Corporation, on behalf of The University of Notre Dame, University of Minnesota and University of Virginia. This paper includes data collected by the K2 mission. Funding for the K2 mission is provided by the NASA Science Mission directorate. This work is based in part

on observations made with the Spitzer Space Telescope, which was operated by the Jet Propulsion Laboratory, California Institute of Technology under a contract with NASA. This work has made use of data from the European Space Agency (ESA) mission Gaia (<https://www.cosmos.esa.int/gaia>), processed by the Gaia Data Processing and Analysis Consortium (DPAC, <https://www.cosmos.esa.int/web/gaia/dpac/consortium>). Funding for the DPAC has been provided by national institutions, in particular the institutions participating in the Gaia Multilateral Agreement.

The authors wish to recognize and acknowledge the very significant cultural role and reverence that the summit of Maunakea has always had within the indigenous Hawaiian community. We are most fortunate to have the opportunity to conduct observations from this mountain.

Facility: Keck:I (HIRES), LBT (PEPSI), FLWO1.5 m (TRES), Kepler, Spitzer.

Software: astropy (Astropy Collaboration et al. 2013, 2018), celerite2 (Foreman-Mackey et al. 2017; Foreman-Mackey 2018), everest (Luger et al. 2016, 2018), exoplanet (Foreman-Mackey et al. 2019, 2021), jupyter (Kluyver et al. 2016), matplotlib (Hunter 2007), misstb (Johnson et al. 2017), numpy (van der Walt et al. 2011), pandas (pandas development team 2020; Wes McKinney 2010), pymc3 (Salvatier et al. 2016), seaborn (Waskom et al. 2017), starry (Luger et al. 2019), theano (Theano Development Team 2016).

Appendix A Derivation of the Mutual Inclination Formula

Here we present the derivation of the formula giving the mutual inclination i_{mut} between the orbits of two planets 1, 2 with orbital inclinations i_1 , i_2 and sky-projected spin-orbit misalignments λ_1 , λ_2 .

We define a coordinate system xyz such that the z axis is along the line of sight and the y axis is parallel to the projected stellar spin axis. Let \hat{y}_n be a unit vector along the orbital angular

momentum of planet n . Let us begin with a system where the orbital plane is parallel to the line of sight and with zero obliquity. For an arbitrary system configuration, we need to rotate \hat{y}_n to the actual orientation of the planetary orbit. We can accomplish this rotation by first rotating the vector by $\pi/2 - i_n$ about the x axis to account for the mutual inclination, and then by λ_n about the z axis to account for the projected obliquity:

$$\hat{y}'_n = R_z(-\lambda_n)R_x(\pi/2 - i_n)\hat{y}_n \quad (\text{A1})$$

where R_z and R_x are rotation matrices about the z and x axes, respectively. The angle between the vectors for the two planets is then

$$\cos i_{\text{mut}} = \hat{y}_1'^T \cdot \hat{y}'_2. \quad (\text{A2})$$

Working through these equations then yields

$$\cos i_{\text{mut}} = \sin i_1 \sin i_2 \cos(\lambda_1 - \lambda_2) + \cos i_1 \cos i_2. \quad (\text{A3})$$

In the case that both planetary orbits are edge-on ($i_1 = i_2 = 90^\circ$), the mutual inclination is simply the difference in the spin-orbit angles:

$$\cos i_{\text{mut}} = \cos(\lambda_1 - \lambda_2). \quad (\text{A4})$$

In the case that both projected spin-orbit angles are identical, the mutual inclination is simply the difference in inclinations:

$$\cos i_{\text{mut}} = \cos(i_1 - i_2). \quad (\text{A5})$$

Appendix B RVRM Tables

We show the priors used in our MCMC analysis of the RVRM data (described in Section 3.3) in Table 4, and list the results and summary statistics from this MCMC in Table 5.

Table 4
Priors Used in the RVRM Analyses

Parameter	Prior	Models
M_* (M_\odot)	$\mathcal{N}(1.10, 0.05)$	L/Q/GP
R_* (R_\odot)	$\mathcal{N}(1.305, 0.07)$	L/Q/GP
P (d)	$\mathcal{N}(24.141445, 0.000056)$	L/Q/GP
T0 - offset (d)	$\mathcal{N}(0, 0.1)$	L/Q/GP
R_P/R_*	$\mathcal{U}(0.0, 0.2)$	L/Q/GP
σ_{Spitzer} (ppt)	$\mathcal{N}(0, 10)$	L/Q/GP
σ_{Kepler} (ppt)	$\mathcal{N}(0, 10)$	L/Q/GP
$\ln \text{jitter}_{\text{Spitzer}}$ (nat)	$\mathcal{U}(-10, 2)$	L/Q/GP
$\ln \text{jitter}_{\text{Kepler}}$ (nat)	$\mathcal{U}(-10, 2)$	L/Q/GP
$v \sin(i_*)$ (km s $^{-1}$)	$\mathcal{N}(24.9, 0.2)$	L/Q/GP
$\cos(i_*)$	$\mathcal{U}(0, 1)$	L/Q/GP
P_{rot} (d)	$\mathcal{N}(2.87, 0.022 \text{ or } 0.2)^*$	L/Q/GP
λ (rad)	$\mathcal{U}(-\pi, \pi)$	L/Q/GP
c_0 (m s $^{-1}$)	$\mathcal{N}(0, 10^5)$	L/Q
c_1 (m s $^{-1}$ d $^{-1}$)	$\mathcal{N}(0, 10^5)$	L/Q
c_2 (m s $^{-1}$ d $^{-2}$)	$\mathcal{N}(0, 10^5)$	Q
$\ln \text{jitter}_{\text{HIRES}}$ (nat)	$\mathcal{N}(\ln(\sigma_{\text{HIRES}}), 5)$	GP
$\ln \text{jitter}_{\text{TRES}}$ (nat)	$\mathcal{N}(\ln(\sigma_{\text{TRES}}), 5)$	GP
$\ln \text{jitter}_{\text{PEPSI}}$ (nat)	$\mathcal{N}(\ln(\sigma_{\text{PEPSI}}), 5)$	GP
μ_{HIRES} (m s $^{-1}$)	$\mathcal{N}(0, 50)$	GP
μ_{TRES} (m s $^{-1}$)	$\mathcal{U}(-1000, 1000)$	GP
μ_{PEPSI} (m s $^{-1}$)	$\mathcal{N}(-1000, 1000)$	GP
$\ln \sigma_{\text{rot}}$ (nat)	$\mathcal{N}(\ln(\sigma_{\text{RV}}), 10)$	GP
$\ln Q_0$ (nat)	$\mathcal{N}(1, 10)$	GP
$\ln \Delta Q$ (nat)	$\mathcal{N}(2, 10)$	GP
f	$\mathcal{U}(0.1, 1)$	GP

Note. $\mathcal{N}(\mu, \sigma)$ denotes a normal prior with mean μ , and standard deviation σ . $\mathcal{U}(a, b)$ denotes a uniform prior with lower limit a and upper limit b . Impact parameter was sampled jointly with R_P/R_* using the Espinoza (2018) formalism. Limb-darkening coefficients in the Kepler and Spitzer bandpasses were sampled from the uninformative priors suggested by Kipping (2013). L: linear model, Q: quadratic model, GP: quasiperiodic Gaussian process. *The width of the P_{rot} prior is given for the tight and loose priors, respectively.

Table 5
MCMC Summary Statistics for the Quasiperiodic GP Model with a Tight P_{rot} Prior (HIRES Data Only)

Parameter	Mean	Std. dev.	HDI (3%)	HDI (97%)	\hat{R}
Period, P (d)	24.141341	0.000023	24.141298	24.141385	1.0000
Time of mid-transit - offset, T_0 (d)	-0.0054	0.0013	-0.0080	-0.0031	0.9998
$\ln \sigma_{\text{rot}}$	5.53	0.53	4.57	6.54	1.0009
$\ln Q_0$	7.7	6.5	-1.8	20.0	1.0001
$\ln \Delta Q$	2.0	9.9	-18.1	19.4	0.9998
M_* (M_\odot)	1.135	0.047	1.050	1.228	1.0000
R_* (R_\odot)	1.407	0.018	1.375	1.441	1.0006
Radius ratio, R_P/R_*	0.071998	0.00062	0.070847	0.073131	1.0000
Impact parameter, b	0.564	0.026	0.515	0.613	1.0000
Limb-darkening parameter u_0	0.54	0.23	0.09	0.93	1.0003
Limb-darkening parameter u_1	-0.03	0.27	-0.47	0.47	1.0017
Limb-darkening parameter $u_{\text{Spitzer},1}$	0.56	0.14	0.27	0.79	1.0001
Limb-darkening parameter $u_{\text{Spitzer},2}$	-0.15	0.18	-0.40	0.20	1.0003
$\ln \text{jitter}_{\text{Spitzer}}$	-5.9	2.3	-9.8	-2.2	1.0006
$v \sin(i_*)$ (km s $^{-1}$)	24.77	0.19	24.40	25.12	1.0010
$\cos(i_*)$	0.085	0.062	0.000015	0.196	1.0014
$\sin(i_*)$	0.9944	0.0072	0.9805	1.0000	1.0014
i_* (deg)	85.1	3.6	78.7	90.0	1.0014
v_{eq} (km s $^{-1}$)	24.91	0.26	24.44	25.41	1.0005
a/R_*	26.06	0.46	25.14	26.87	0.9998
$\cos(i_{\text{pl}})$	0.0217	0.0013	0.0190	0.0241	0.9998
i_{pl} (deg)	88.759	0.077	88.620	88.911	0.9998
λ (rad)	0.14	0.27	-0.23	0.74	1.0002
λ (deg)	8	15	-13	42	1.0002
f	0.57	0.25	0.17	1.0	0.9999

Note. HDI: highest density interval. \hat{R} : Gelman–Rubin statistic. The reference time T_0 indicates the time of mid-transit relative to the date BJD = 2458781.089056.

Appendix C Corner Plots

In this Appendix we present the corner plots from our fits to determine the age of V1298 Tau (Section 3.1) and measure the

spin–orbit alignment of the planet (Section 3.3). We show these plots in Figures 9 and 10, respectively.

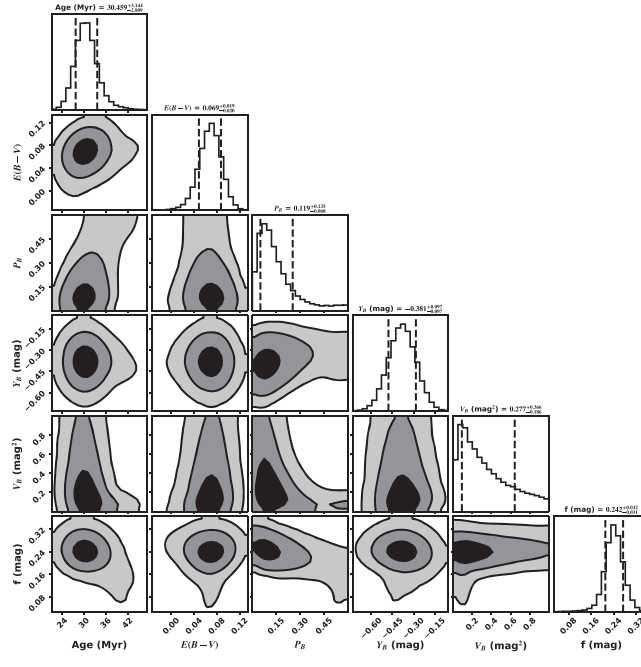


Figure 9. Corner plot from the Markov chain Monte Carlo posteriors for fitting the age of V1298 Tau. We show all six fit parameters. P_B , V_B , and Y_B are parameters that describe the outlier population, age and $E(B - V)$ describe the primary population, and f applies to all stars in the sample (treated as a missing uncertainty). Similar fits using the Dartmouth Stellar Evolution Program magnetic models and with modified sample selection yield similar ages and reddening, but different outlier population parameters.

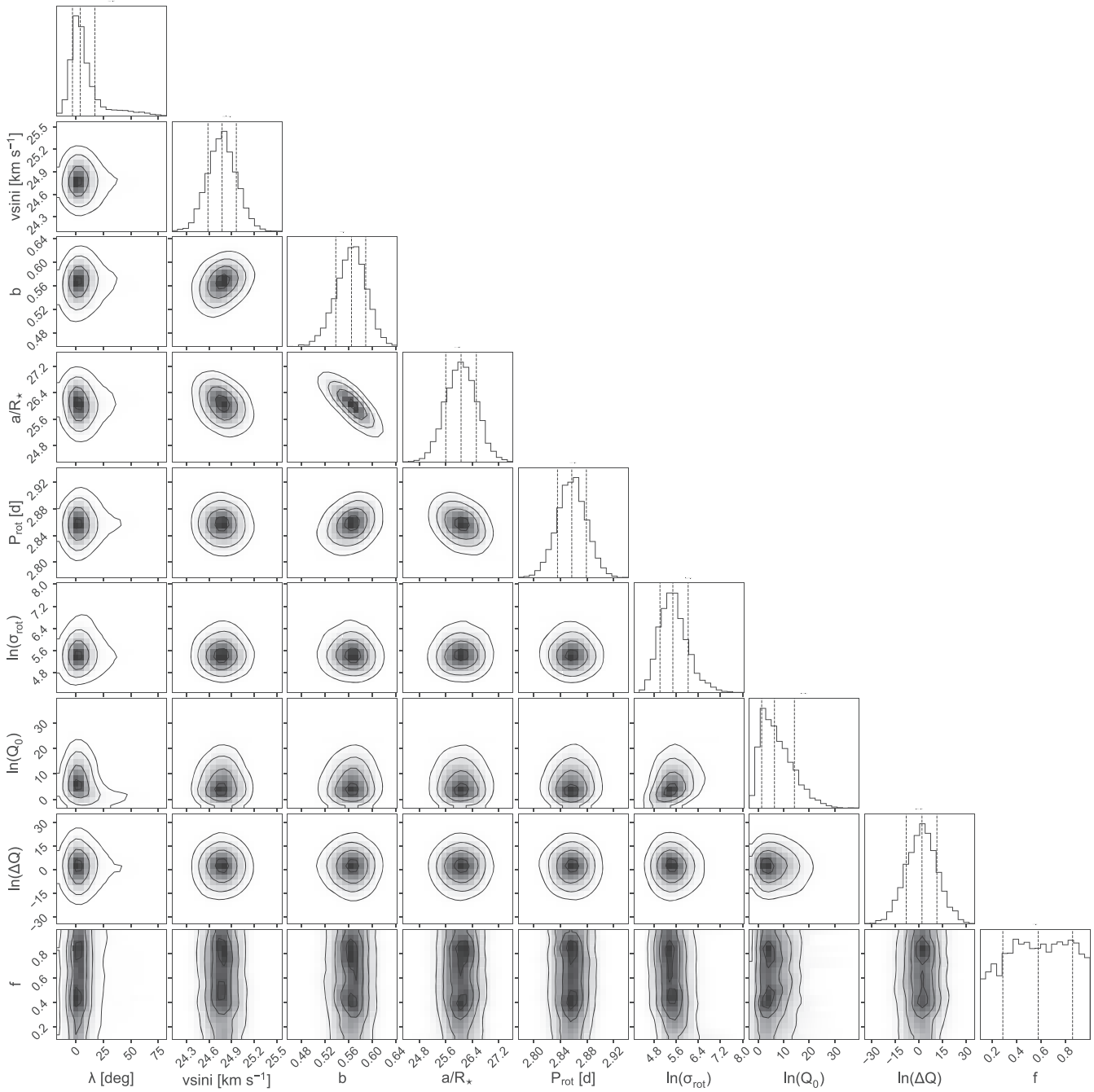


Figure 10. Posterior parameter distributions for the RM fit with the quasiperiodic GP + RM model with a tight P_{rot} prior (for the HIRES data only). This is our adopted model.

ORCID iDs

Marshall C. Johnson [ID](https://orcid.org/0000-0002-5099-8185) <https://orcid.org/0000-0002-5099-8185>
 Trevor J. David [ID](https://orcid.org/0000-0001-6534-6246) <https://orcid.org/0000-0001-6534-6246>
 Erik A. Petigura [ID](https://orcid.org/0000-0003-0967-2893) <https://orcid.org/0000-0003-0967-2893>
 Howard T. Isaacson [ID](https://orcid.org/0000-0002-0531-1073) <https://orcid.org/0000-0002-0531-1073>
 Judah Van Zandt [ID](https://orcid.org/0000-0002-4290-6826) <https://orcid.org/0000-0002-4290-6826>
 Ilya Ilyin [ID](https://orcid.org/0000-0002-0551-046X) <https://orcid.org/0000-0002-0551-046X>
 Klaus Strassmeier [ID](https://orcid.org/0000-0002-6192-6494) <https://orcid.org/0000-0002-6192-6494>
 Matthias Mallonn [ID](https://orcid.org/0000-0003-2865-042X) <https://orcid.org/0000-0003-2865-042X>
 Andrew W. Mann [ID](https://orcid.org/0000-0003-3654-1602) <https://orcid.org/0000-0003-3654-1602>
 John H. Livingston [ID](https://orcid.org/0000-0002-4881-3620) <https://orcid.org/0000-0002-4881-3620>
 Rodrigo Luger [ID](https://orcid.org/0000-0002-0296-3826) <https://orcid.org/0000-0002-0296-3826>

Fei Dai [ID](https://orcid.org/0000-0002-8958-0683) <https://orcid.org/0000-0002-8958-0683>
 Lauren M. Weiss [ID](https://orcid.org/0000-0002-3725-3058) <https://orcid.org/0000-0002-3725-3058>
 Teo Močnik [ID](https://orcid.org/0000-0003-4603-556X) <https://orcid.org/0000-0003-4603-556X>
 Steven Giacalone [ID](https://orcid.org/0000-0002-8965-3969) <https://orcid.org/0000-0002-8965-3969>
 Michelle L. Hill [ID](https://orcid.org/0000-0002-0139-4756) <https://orcid.org/0000-0002-0139-4756>
 Malena Rice [ID](https://orcid.org/0000-0002-7670-670X) <https://orcid.org/0000-0002-7670-670X>
 Sarah Blunt [ID](https://orcid.org/0000-0002-3199-2888) <https://orcid.org/0000-0002-3199-2888>
 Ryan Rubenzahl [ID](https://orcid.org/0000-0003-3856-3143) <https://orcid.org/0000-0003-3856-3143>
 Paul A. Dalba [ID](https://orcid.org/0000-0002-4297-5506) <https://orcid.org/0000-0002-4297-5506>
 Gilbert A. Esquerdo [ID](https://orcid.org/0000-0002-9789-5474) <https://orcid.org/0000-0002-9789-5474>
 Michael L. Calkins [ID](https://orcid.org/0000-0002-2830-5661) <https://orcid.org/0000-0002-2830-5661>
 Daniel Foreman-Mackey [ID](https://orcid.org/0000-0002-9328-5652) <https://orcid.org/0000-0002-9328-5652>

References

- Addison, B. C., Horner, J., Wittenmyer, R. A., et al. 2021b, *AJ*, **162**, 137
- Addison, B. C., Knudstrup, E., Wong, I., et al. 2021a, *AJ*, **162**, 292
- Ahlers, J. P., Johnson, M. C., Stassun, K. G., et al. 2020, *AJ*, **160**, 4
- Albrecht, S., Reffert, S., Snellen, I., Quirrenbach, A., & Mitchell, D. S. 2007, *A&A*, **474**, 565
- Albrecht, S., Winn, J. N., Johnson, J. A., et al. 2012, *ApJ*, **757**, 18
- Angus, R., Morton, T., Aigrain, S., Foreman-Mackey, D., & Rajpaul, V. 2018, *MNRAS*, **474**, 2094
- Astropy Collaboration, Price-Whelan, A. M., Sipócz, B. M., et al. 2018, *AJ*, **156**, 123
- Astropy Collaboration, Robitaille, T. P., Tollerud, E. J., et al. 2013, *A&A*, **558**, A33
- Bailey, E., Batygin, K., & Brown, M. E. 2016, *AJ*, **152**, 126
- Bate, M. R., Lodato, G., & Pringle, J. E. 2010, *MNRAS*, **401**, 1505
- Batygin, K. 2012, *Natur*, **491**, 418
- Batygin, K., & Adams, F. C. 2013, *ApJ*, **778**, 169
- Batygin, K., Adams, F. C., Batygin, Y. K., & Petigura, E. A. 2020, *AJ*, **159**, 101
- Batygin, K., Morbidelli, A., & Tsiganis, K. 2011, *A&A*, **533**, A7
- Bedell, M., Hogg, D. W., Foreman-Mackey, D., Montet, B. T., & Luger, R. 2019, *AJ*, **158**, 164
- Benatti, S., Damasso, M., Borsa, F., et al. 2021, *A&A*, **650**, 66
- Berdugina, S. V., & Usoskin, I. G. 2003, *A&A*, **405**, 1121
- Bourrier, V., Lovis, C., Beust, H., et al. 2018, *Natur*, **553**, 477
- Bourrier, V., Lovis, C., Cretignier, M., et al. 2021, *A&A*, **654**, A152
- Bressan, A., Marigo, P., Girardi, L., et al. 2012, *MNRAS*, **427**, 127
- Buchhave, L. A., Latham, D. W., Johansen, A., et al. 2012, *Natur*, **486**, 375
- Collier Cameron, A., Guenther, E., Smalley, B., et al. 2010, *MNRAS*, **407**, 507
- Dai, F., Roy, A., Fulton, B., et al. 2020, *AJ*, **160**, 193
- Dalal, S., Hébrard, G., Lecavelier des Étangs, A., et al. 2019, *A&A*, **631**, A28
- David, T. J., Cody, A. M., Hedges, C. L., et al. 2019a, *AJ*, **158**, 79
- David, T. J., Petigura, E. A., Luger, R., et al. 2019b, *ApJL*, **885**, L12
- Dawson, R. I., & Johnson, J. A. 2018, *ARA&A*, **56**, 175
- Dholakia, S., Dholakia, S., Cody, A. M., et al. 2019, *PASP*, **131**, 114402
- Donati, J.-F., Semel, M., Carter, B. D., Rees, D. E., & Collier Cameron, A. 1997, *MNRAS*, **291**, 658
- Dotter, A., Chaboyer, B., Jevremović, D., et al. 2008, *ApJS*, **178**, 89
- Espinosa, N. 2018, *RNAAS*, **2**, 209
- Fabrycky, D., & Tremaine, S. 2007, *ApJ*, **669**, 1298
- Fabrycky, D. C., & Winn, J. N. 2009, *ApJ*, **696**, 1230
- Feiden, G. A., & Chaboyer, B. 2012, *ApJ*, **761**, 30
- Feinstein, A. D., Montet, B. T., Johnson, M. C., et al. 2021, *AJ*, **162**, 213
- Fürész, G. 2008, PhD thesis, Univ. of Szeged, Hungary, http://doktori.bibl.u-szeged.hu/id/eprint/1135/1/gabor_furesz_thesis.pdf
- Fielding, D. B., McKee, C. F., Socrates, A., Cunningham, A. J., & Klein, R. I. 2015, *MNRAS*, **450**, 3306
- Foreman-Mackey, D. 2018, *RNAAS*, **2**, 31
- Foreman-Mackey, D., Agol, E., Ambikasaran, S., & Angus, R. 2017, *AJ*, **154**, 220
- Foreman-Mackey, D., Barentsen, G., & Barclay, T. 2019, dfm/exoplanet: exoplanet v0.1.5, doi:[10.5281/zenodo.2587222](https://doi.org/10.5281/zenodo.2587222)
- Foreman-Mackey, D., Hogg, D. W., Lang, D., & Goodman, J. 2013, *PASP*, **125**, 306
- Foreman-Mackey, D., Luger, R., Agol, E., et al. 2021, *JOSS*, **6**, 3285
- Foucart, F., & Lai, D. 2011, *MNRAS*, **412**, 2799
- Gaia Collaboration, Brown, A. G. A., Vallenari, A., et al. 2021, *A&A*, **649**, A1
- Gaia Collaboration, Prusti, T., de Bruijne, J. H. J., et al. 2016, *A&A*, **595**, A1
- Gaudi, B. S., Stassun, K. G., Collins, K. A., et al. 2017, *Natur*, **546**, 514
- Gelman, A., & Rubin, D. B. 1992, *StaSc*, **7**, 457
- Gomes, R., Deienno, R., & Morbidelli, A. 2017, *AJ*, **153**, 27
- Heitzmann, A., Zhou, G., Quinn, S. N., et al. 2021, *ApJ*, **922**, 1
- Heller, C. H. 1993, *ApJ*, **408**, 337
- Hirano, T., Krishnamurthy, V., Gaidos, E., et al. 2020, *ApJL*, **899**, L13
- Hjorth, M., Albrecht, S., Hirano, T., et al. 2021, *PNAS*, **118**, 2017418118
- Hogg, D. W., Bovy, J., & Lang, D. 2010, arXiv:1008.4686
- Howard, A. W., Johnson, J. A., Marcy, G. W., et al. 2010, *ApJ*, **721**, 1467
- Howell, S. B., Sobeck, C., Haas, M., et al. 2014, *PASP*, **126**, 398
- Huber, D., Carter, J. A., Barbieri, M., et al. 2013, *Sci*, **342**, 331
- Hunter, J. D. 2007, *CSE*, **9**, 90
- Ilyin, I. V. 2000, PhD thesis, University of Oulu Finland
- Johnson, M. C., Cochran, W. D., Addison, B. C., Tinney, C. G., & Wright, D. J. 2017, *AJ*, **154**, 137
- Johnson, M. C., Cochran, W. D., Albrecht, S., et al. 2014, *ApJ*, **790**, 30
- Johnson, M. C., Cochran, W. D., Collier Cameron, A., & Bayliss, D. 2015, *ApJL*, **810**, L23
- Johnson, M. C., Rodriguez, J. E., Zhou, G., et al. 2018, *AJ*, **155**, 100
- Kipping, D. M. 2013, *MNRAS*, **435**, 2152
- Kluyver, T., Ragan-Kelley, B., Pérez, F., et al. 2016, in Positioning and Power in Academic Publishing: Players, Agents and Agendas, ed. F. Loizides & B. Schmidt (Amsterdam: IOS Press), 87
- Krolkowski, D. M., Kraus, A. L., & Rizzuto, A. C. 2021, *AJ*, **162**, 110
- Kuiper, G. P. 1951, *PNAS*, **37**, 1
- Lai, D. 2014, *MNRAS*, **440**, 3532
- Lai, D., Foucart, F., & Lin, D. N. C. 2011, *MNRAS*, **412**, 2790
- Luger, R., Agol, E., Foreman-Mackey, D., et al. 2019, *AJ*, **157**, 64
- Luger, R., Agol, E., Kruse, E., et al. 2016, *AJ*, **152**, 100
- Luger, R., Kruse, E., Foreman-Mackey, D., Agol, E., & Saunders, N. 2018, *AJ*, **156**, 99
- Luhman, K. L. 2018, *AJ*, **156**, 271
- Lund, M. B., Rodriguez, J. E., Zhou, G., et al. 2017, *AJ*, **154**, 194
- Mann, A. W., Johnson, M. C., Vanderburg, A., et al. 2020, *AJ*, **160**, 179
- Marsden, S. C., Donati, J. F., Semel, M., Petit, P., & Carter, B. D. 2006, *MNRAS*, **370**, 468
- Marsden, S. C., Jardine, M. M., Ramírez Vélez, J. C., et al. 2011, *MNRAS*, **413**, 1939
- Martioli, E., Hébrard, G., Moutou, C., et al. 2020, *A&A*, **641**, L1
- McKinney, W. 2010, in Proc. 9th Python in Science Conf., ed. S. van der Walt & J. Millman, 56
- Millholland, S., & Batygin, K. 2019, *ApJ*, **876**, 119
- Montet, B. T., Feinstein, A. D., Luger, R., et al. 2020, *AJ*, **159**, 112
- Naoz, S., Farr, W. M., Lithwick, Y., Rasio, F. A., & Teyssandier, J. 2011, *Natur*, **473**, 187
- Palle, E., Oshagh, M., Casasayas-Barris, N., et al. 2020, *A&A*, **643**, A25
- pandas development team, T. 2020, pandas-dev/pandas: Pandas, Zenodo, doi:[10.5281/zenodo.3509134](https://doi.org/10.5281/zenodo.3509134)
- Rubenzahl, R. A., Dai, F., Howard, A. W., et al. 2021, *AJ*, **161**, 119
- Salvatier, J., Wiecki, T. V., & Fonnesbeck, C. 2016, *PeerJ Comp. Sci.*, **2**, e55
- Sanchis-Ojeda, R., Winn, J. N., Marcy, G. W., et al. 2013, *ApJ*, **775**, 54
- Spalding, C. 2019, *ApJ*, **879**, 12
- Spalding, C., & Batygin, K. 2014, *ApJ*, **790**, 42
- Spalding, C., & Batygin, K. 2015, *ApJ*, **811**, 82
- Storch, N. I., Anderson, K. R., & Lai, D. 2014, *Sci*, **345**, 1317
- Strassmeier, K. G., Ilyin, I., Järvinen, A., et al. 2015, *AN*, **336**, 324
- Strassmeier, K. G., Ilyin, I., & Steffen, M. 2018, *A&A*, **612**, A44
- Su, Y., & Lai, D. 2020, *ApJ*, **903**, 7
- Suárez Mascareño, A., Damasso, M., Lodieu, N., et al. 2021, *NatAs*, **6**, 232
- Theano Development Team 2016, arXiv:1605.02688
- Thies, I., Kroupa, P., Goodwin, S. P., Stamatellos, D., & Whitworth, A. P. 2011, *MNRAS*, **417**, 1817
- Tofflemire, B. M., Rizzuto, A. C., Newton, E. R., et al. 2021, *AJ*, **161**, 171
- Tran, Q. H., Bowler, B. P., Cochran, W. D., et al. 2021, *AJ*, **161**, 173
- Tremaine, S. 1991, *Icar*, **89**, 85
- van der Walt, S., Colbert, S. C., & Varoquaux, G. 2011, *CSE*, **13**, 22
- Vogt, S. S., Allen, S. L., Bigelow, B. C., et al. 1994, *Proc. SPIE*, **2198**, 362
- Waskom, M., Botvinnik, O., O’Kane, D., et al. 2017, mwaskom/seaborn: v0.8.1, doi:[10.5281/zenodo.883859](https://doi.org/10.5281/zenodo.883859)
- Winn, J. N., Johnson, J. A., Howard, A. W., et al. 2010, *ApJL*, **723**, L223
- Wirth, C. P., Zhou, G., Quinn, S. N., et al. 2021, *ApJL*, **917**, L34
- Wu, Y., Murray, N. W., & Ramsahai, J. M. 2007, *ApJ*, **670**, 820
- Zhou, G., Winn, J. N., Newton, E. R., et al. 2020, *ApJL*, **892**, L21
- Ziegler, C., Tokovinin, A., Briceño, C., et al. 2020, *AJ*, **159**, 19